OPEN ACCESS

Modeling the Morphological Effects of Catalyst and Ionomer Loading on Porous Carbon Supports of PEMFC

Journal of The Electrochemical Society, 2022 **169** 034509

Modeling the Morphological Effects of Catalyst and Ionomer Loading on Porous Carbon Supports of PEMFC

Anne-Christine Scherzer,[1,z] Patrick Schneider,[1] Patrick K. Herring,[2] Matthias Klingele,[1] Nada Zamel,[1] and Dietmar Gerteisen[1]

[1]*Fraunhofer Institute for Solar Energy Systems ISE, 79110 Freiburg, Germany*
[2]*Toyota Research Institute, One Kendall Square, Cambridge, Massachusetts 02139, United States of America*

We present a model of the cathode catalyst layer morphology before and after loading a porous catalyst support with Pt and ionomer. Support nanopores and catalyst particles within pores and on the support surface are described by size distributions, allowing for qualitative processes during the addition of a material phase to be dependent on the observed pore and particle size. A particular focus is put on the interplay of pore impregnation and blockage due to ionomer loading and the consequences for the Pt/ionomer interface, ionomer film thickness and protonic binding of particles within pores. We used the model to emulate six catalyst/support combinations from literature with different porosity, surface area and pore size distributions of the support as well as varying particle size distributions and ionomer/carbon ratios. Besides providing qualitatively and quantitatively accurate predictions, the model is able to explain why the protonically active catalyst surface area has been reported to not increase monotonically with ionomer addition for some supports, but rather decrease again when the optimum ionomer content is exceeded. The proposed model constitutes a fast translation from manufacturing parameters to catalyst layer morphology which can be incorporated into existing performance and degradation models in a straightforward way.
 [DOI: 10.1149/1945-7111/ac58c2]

Manuscript submitted December 10, 2021; revised manuscript received January 31, 2022. Published March 7, 2022.

List of symbols

Subscripts

C	Carbon support
cat	Catalyst powder (Pt and C)
ccl	Referring to entire CCL
inner	Inside support primary particle nanopores, referring to entire CCL
io	Ionomer
outer	On support primary particle surface, referring to entire CCL
p	Primary pore
Pt	Platinum catalyst
Pt/C	After loading the support with Pt
Pt/C/io	After loading the support with Pt and ionomer
total	Referring to the entire CCL

Parameters

ρ	Material density, kg m^{-3}
Θ	Fractional coverage referring to available interfacial surface
A	Area, m^2
d	Layer thickness, m
L	Catalyst loading, kg m^{-2}
l	Length, m
m	Mass, kg
N	Dimensionless number of particles or pores
n'	Particle or pore number distribution, m^{-1}
n''	Distribution of particles in pores, m^{-1}m^{-1}
r	Particle or pore radius, m
V	Volume, m^3
v'	Particle or pore volume distribution, m^{3}m^{-1}
wt	Dimensionless mass fraction
x	Dimensionless fraction or partition

On the way to optimizing fuel cell performance and cost, it is vital to design the cathode catalyst layer (CCL) such that maximum catalyst utilization can be obtained. A performant CCL morphology provides a high electrochemically active surface area (ECSA) and good protonic binding of the catalyst through contact with the ionomer while maintaining sufficient oxygen supply to avoid mass transport limitations. In this context, highly porous carbon supports have come to play an important role as their internal nanopores strongly increase the surface area on which catalyst particles can be dispersed. Literature has provided evidence that the partition of catalyst particles located inside the support primary pores increases with support porosity. Further, particles inside primary pores tend to be smaller than those located on the support surface.[1–3] Both of these facts lead to the trend that a relatively higher catalyst activity and specific surface area is contributed by the particles inside pores as the support becomes more porous.

At the same time, the protonic connectivity of the catalyst particles within the pores remains a matter of discussion. While it is generally agreed that water in the pores can provide a protonic pathway to these particles,[3–6] there are contradictory opinions as to whether or not the particles can be contacted directly by ionomer. Uchida and co-workers[7] reported that increasing the ionomer content linearly decreased the secondary pore volume constituted by pores >40 nm, but did not affect the volume of pores between 20 and 40 nm in diameter. Contrarily, Soboleva and co-workers found that the volume of pores between 2 and 20 nm decreased asymptotically with ionomer addition while that of pores larger than 50 nm was only significantly decreased at the highest investigated ionomer content.[8] The volume of nanopores below 2 nm decreased as well which was taken to be caused by excess ionomer blocking the entrances of these pores rather than impregnating them, a process which was also postulated in other works.[3,9] However, recent publications[1,2] suggest that, for highly porous supports, some portion of the ionomer can actually penetrate pores <10 nm and enhance the electrochemical contribution of the catalyst particles within. While this is desirable, it is unclear what the optimum extent of pore impregnation is and how exactly it can be achieved while avoiding pore blockage. Some groups found that increasing the Nafion content improved the ionomer coverage on Pt on porous supports,[10,11] but others found that the coverage remained largely

[z]E-mail: anne-christine.scherzer@ise.fraunhofer.de

constant with additional ionomer.[12] Contact angle studies by Andersen et al. suggested an increase in coverage up to an optimum ionomer content of 30 wt%, but a tendency for ionomer aggregation at higher ionomer contents with subsequent loss of interfacial area to Pt.[13] Further, some authors found that the ionomer film thickness on Pt increased with I/C ratio[10,14,15] while others derived that the thickness remains constant at intermediate I/C ratios and only increases upon very high ionomer contents.[11]

These uncertainties notwithstanding, is evident that support porosity, amount and size of catalyst particles on the support surface and within the pores as well as the amount and film thickness of the ionomer and the available Pt/ionomer interface play a role in both fuel cell performance and durability.[1,2,13,16–18] Accessing these parameters for a given CCL is important for understanding and optimizing electrochemical processes within. Many previous works thus address one or several of said morphological properties, for instance using physical models of porous supports[19] or water-filled agglomerates,[5,6] pore-network models,[20] molecular dynamics approaches[4] or models based on microstructure reconstruction.[21–24] Where these abstractions of the CCL morphology become complex or computationally expensive, machine learning and artificial intelligence methods are employed to assist in CCL reconstruction, control and optimization.[25] The various approaches have been able to provide valuable insights into ionomer coverage on Pt and carbon,[22,23] pore volume loss due to ionomer loading,[20] ionomer film thickness distribution[15,22] and the impact of ionomer content on Pt utilization[6] or cell performance,[5,15,23] often for different types of carbon support, to name only a few aspects.

The intention of this work is to contribute a fast morphological model which simultaneously accounts for pore and particle size distributions and their effect on ionomer distribution within the support, particularly regarding the interplay of pore impregnation and blockage. The model allows to derive morphological properties unique to the given support/Pt/ionomer system on primary pore and particle level. These include experimentally hard to access parameters such as the available Pt/ionomer interface, ionomer film thickness and protonic binding of particles within pores. Further, the obtained pore-scale properties can be summarized to provide characteristics of the full CCL such as support surface area and remaining pore volume after Pt and ionomer addition, offering a variety of parameters for validation. We present the model with the twofold aim of establishing theoretical correspondence to trends observed in recent literature[1,2] and providing a general framework for translating manufacturing properties of CCLs with porous supports to morphological features that can be integrated into existing performance and degradation models.

Modeling

In the following, we establish a mathematical description of the CCL morphology by combining considerations for the different material phases. We begin with the description of the porous carbon support and subsequently proceed to the distribution of catalyst particles and ionomer on the support surface and within the nanopores.

Porous carbon support.—We consider a CCL of constant thickness d_{ccl} spread over the cell active area A_{ccl} and hence with the volume

$$V_{ccl} = A_{ccl} d_{ccl} \quad [1]$$

From the given platinum loading L_{Pt}, we can calculate the total Pt mass within the CCL

$$m_{Pt,total} = L_{Pt} A_{ccl} \quad [2]$$

and subsequently the total mass of solid carbon

$$m_{C,total} = \frac{m_{Pt,total}}{wt_{Pt/C}} \quad [3]$$

where $wt_{Pt/C}$ is the weight percentage of the catalyst compared to the support for the given CCL. Note many sources provide the weight percentage

$$wt_{Pt/cat} = \frac{m_{Pt,total}}{m_{Pt,total} + m_{C,total}} \quad [4]$$

instead of $wt_{Pt/C}$, in which case the latter can be obtained as

$$wt_{Pt/C} = \frac{wt_{Pt,cat}}{1 - wt_{Pt,cat}} \quad [5]$$

We assume that the catalyst support structure consists of spherical carbon primary particles of radius r_C which feature multiple nanopores. Assuming that, on average, a certain partition $x_{C,p}$ of the sphere volume is devoted to nanopores, the total number of primary particles within the CCL for a given carbon mass is

$$N_C = \frac{m_{C,total}}{\frac{4}{3}\pi r_C^3 \rho_C (1 - x_{C,p})} \quad [6]$$

where ρ_C is the density of the solid carbon phase. The overall volume taken up by solid carbon and nanopores is hence

$$V_{C,total} = \frac{4}{3}\pi r_C^3 N_C \quad [7]$$

and the overall nanopore volume is

$$V_{p,total} = x_{C,p} V_{C,total} \quad [8]$$

In most cases, the specific pore volume $V_{p,total}/m_{C,total}$ is given by experimental data and can be used to calculate $x_{C,p}$ by combining Eqs. 6 to 8

$$x_{C,p} = \frac{1}{1 + m_{C,total}(\rho_C V_{p,total})^{-1}} \quad [9]$$

If there is no information available on the CCL thickness d_{ccl}, we propose to estimate this value from the obtained number of carbon primary particles in an approach similar to that of Darling.[26] Assuming a certain packing density $x_{C,pack} < 0.74$ where the latter is the maximum packing density of spheres, d_{ccl} is calculated as

$$d_{ccl} = \frac{1}{x_{C,pack}} \frac{V_{C,total}}{A_{ccl}} \quad [10]$$

In this work, we assume nanopores of cylindrical shape and uniform length l_p. The volume of a single pore for a given pore opening radius r_p is hence

$$V_p(r_p) = l_p \pi r_p^2 \quad [11]$$

The surface of the pore walls, excluding the bottom of the pore is

$$A_{p,wall}(r_p) = 2\pi r_p l_p \quad [12]$$

and the surface of the pore opening, which equals that of the pore bottom, is

$$A_{p,opening}(r_p) = \pi r_p^2 \quad [13]$$

We assume a distribution $dn_{p,C}(r_p)/dr_p$ which describes the number of nanopores of a certain size class r_p in the unloaded catalyst support. For simpler notation, we will use the abbreviation

$$n'(r) = \frac{dn(r)}{dr} \quad [14]$$

for distributions throughout this work. In the model, all distributions can either be an analytical relation or discrete values for each size class, e.g. obtained from TEM data. The Eqs. stated in the following refer to a continous distribution, but analogous relations hold for the discrete case with the integrals replaced by an appropriate summation rule. The pore size distribution can either be adapted directly from measured data or be any relation $n'(r_p)$ which is then normalized to

$$n'_{p,C}(r_p) = \frac{V_{p,total}}{\int_0^\infty V_p(\hat{r}_p)n'(\hat{r}_p)d\hat{r}_p} n'(r_p) \quad [15]$$

to ensure that the distribution yields the correct overall pore volume for the given pore morphology. Using this distribution, we can estimate the overall surface area of the catalyst layer. We assume that the carbon surface area of a primary particle which is lost due to a pore opening approximately equals the area gained at the pore bottom. Any surface area increase due to nanopores in otherwise spherical carbon primary particles is then due to the pore walls such that the overall support surface area is calculated as

$$A_{C,total} = 4\pi r_C^2 N_C + \int_0^\infty A_{p,wall}(\hat{r}_p)n'_{p,C}(\hat{r}_p)d\hat{r}_p \quad [16]$$

The pore size distribution of the carbon support before Pt and ionomer loading can be transferred into a pore volume distribution (PVD)

$$v'_{p,C}(r_p) = V(r_p)n'_{p,C}(r_p) \quad [17]$$

which will be used frequently throughout this work. Analogous to Eq. 14, we define $v'(r) = dv(r)/dr$.

Catalyst distribution in pores and on support surface.—Similar to the pore size distribution, we introduce continous or discrete distributions $n'_{Pt,inner}(r_{Pt})$ and $n'_{Pt,outer}(r_{Pt})$ which denote the catalyst particle size distributions inside the nanopores and on the support surface, respectively. The particles are assumed to be spherical with a volume

$$V_{Pt}(r_{Pt}) = \frac{4}{3}\pi r_{Pt}^3 \quad [18]$$

and surface area

$$A_{Pt}(r_{Pt}) = 4\pi r_{Pt}^2 \quad [19]$$

and density ρ_{Pt}. For a given catalyst layer, we assume that a mass fraction $wt_{Pt,inner}$ of the overall Pt loading resides within the support nanopores and obtain appropriately normalized distributions from initially unnormalized relations $n'_{inner}(r_{Pt})$ and $n'_{outer}(r_{Pt})$ as

$$n'_{Pt,inner}(r_{Pt}) = \frac{wt_{Pt,inner}m_{Pt,total}}{\rho_{Pt}\int_0^\infty V_{Pt}(\hat{r}_{Pt})n'_{inner}(\hat{r}_{Pt})d\hat{r}_{Pt}} n'_{inner}(r_{Pt}) \quad [20]$$

and

$$n'_{Pt,outer}(r_{Pt}) = \frac{(1 - wt_{Pt,inner})m_{Pt,total}}{\rho_{Pt}\int_0^\infty V_{Pt}(\hat{r}_{Pt})n'_{outer}(\hat{r}_{Pt})d\hat{r}_{Pt}} n'_{outer}(r_{Pt}) \quad [21]$$

(compare to the approach in Ref. 27). Alternatively, the respective partitions of inner and outer particles may be defined by particle counts (e.g. from STEM data[2]), rather than weight percentages. In this case, $wt_{Pt,inner}$ must be calculated such that, next to normalizing to the overall Pt loading (Eqs. 20 and 21), the measured relation between inner and outer particle numbers is also satisfied

$$\frac{N_{Pt,inner}}{N_{Pt,outer}} = \frac{\int_0^\infty n'_{Pt,inner}(\hat{r}_{Pt})d\hat{r}_{Pt}}{\int_0^\infty n'_{Pt,outer}(\hat{r}_{pt})d\hat{r}_{Pt}} \quad [22]$$

From the normalized distributions, the ECSA can be calculated as

$$A_{Pt,inner} = \int_0^\infty A_{Pt}(\hat{r}_{Pt})n'_{Pt,inner}(\hat{r}_{Pt})d\hat{r}_{Pt} \quad [23]$$

and analogously for the outer Pt.[28] Next, we link the inner Pt particle size distribution to the pore size distribution in order to define how Pt is distributed within the nanopores. A Pt particle of radius r_{Pt} can only be situated in a nanopore of size $r_p \geqslant r_{Pt}$. We assume that inner Pt is distributed according to pore volume, that is, the larger the pore, the more particles can be found there. Among pores of the same size, each pore is attributed the same number of Pt particles. The total number of Pt particles of size r_{Pt} that can be found in the pores of size r_p can hence be described by the two-dimensional distribution

$$n''_{Pt,p}(r_{Pt}, r_p) = \begin{cases} n'_{Pt,inner}(r_{Pt})\dfrac{V_p(r_p)n'_{p,C}(r_p)}{\int_{r_{Pt}}^\infty V_p(\hat{r}_p)n'_{p,C}(\hat{r}_p)d\hat{r}_p} & for\ r_{Pt} \leqslant r_p \\ 0 & otherwise \end{cases} \quad [24]$$

with $n''_{Pt,p}(r_{Pt}, r_p) = dn_{Pt,p}(r_{Pt}, r_p)/dr_{Pt}dr_p$. In the above expression, the factor $V_p(r_p)n'_{p,C}(r_p) \Big/ \int_{r_{Pt}}^\infty V_p(\hat{r}_p)n'_{p,C}(\hat{r}_p)d\hat{r}_p$ compares the differential volume contributed by the observed pore size class r_p with the total volume of pores which are large enough to host a particle of size r_{Pt}. With $n'_{Pt,inner}(r_{Pt})$ corresponding to the total number of particles of size class r_{Pt} slated for distribution into pores with $r_p \geqslant r_{Pt}$, the amount of particles which is attributed to the pore size class r_p then corresponds to $n'_{Pt,inner}(r_{Pt})$ multiplied by the aforementioned factor. The expression $n''_{Pt,p}$ will allow us to derive several quantities of interest throughout this work, one example being the ionomer coverage on Pt particles of a given size within support nanopores.

To conclude this Section, it should be noted that loading Pt into the pores causes the PVD $v'_{p,C}(r_p)$ of the support to change to a different distribution $v'_{p,Pt/C}(r_p)$.[1,2,8] We will illustrate how $v'_{p,Pt/C}$ was obtained from $n''_{Pt,p}$ for different qualitative scenarios in the results part, and assume that $v'_{p,Pt/C}$ is given for the following considerations on ionomer loading.

Ionomer distribution and Pt/ionomer interface.—A central contribution of our model is the calculation of the distribution of available ionomer on the support surface and in the nanopores, depending on the given Pt/C morphology and ionomer loading. The total mass of ionomer within the CCL can be obtained using the weight percentage wt_{io} which links the ionomer mass to that of the Pt/C catalyst

$$m_{io,total} = \frac{wt_{io}}{1 - wt_{io}}(m_{C,total} + m_{Pt,total}) \quad [25]$$

If the ionomer to carbon mass ratio I/C is given instead of wt_{io}, the weight percentage can be derived as

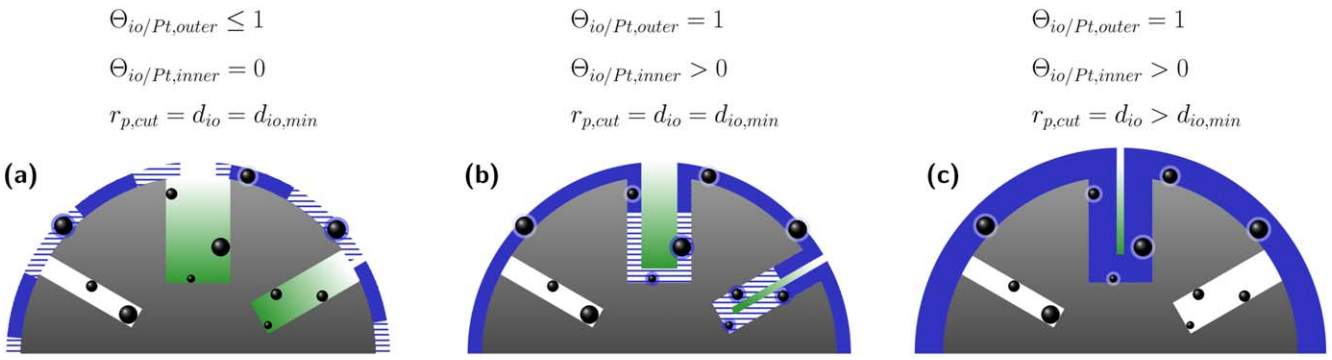

Figure 1. Different ionomer impregnation cases: (a) Case 1 at low I/C; (b) Case 2 at intermediate I/C; (c) Case 3 at high I/C. Grey: carbon primary particle, black: Pt particles, blue: ionomer film. Solid blue color indicates partial ionomer coverage, solid plus hatched blue color indicates maximum possible ionomer coverage in the respective case. Pt particles with blue halo indicate the maximum protonically connected ECSA in the respective case. Green areas indicate accessible pore volume after ionomer loading.

$$wt_{io} = \frac{I/C}{wt_{Pt/C} + I/C + 1} \quad [26]$$

The total ionomer volume for a given ionomer density ρ_{io} is hence

$$V_{io,total} = \frac{m_{io,total}}{\rho_{io}} \quad [27]$$

We assume that the ionomer forms a film of constant thickness d_{io}. In order to calculate how the available ionomer volume is distributed on the support and inside the nanopores, we formulate the schematic proposed by Kobayashi et al.[2] into three qualitative cases:

1. At low ionomer contents, ionomer impregnation sets out on the outer surface of the support primary particles. Ionomer may not penetrate the nanopores until all available outer support surface is covered by an ionomer film with a set minimum thickness $d_{io} = d_{io,\min}$.
2. If full outer coverage with $d_{io} = d_{io,\min}$ is reached, ionomer starts to penetrate nanopores which are sufficiently large, that is, which have pore openings larger than a cutoff radius $r_{p,cut}$ which is considered to equal the film thickness d_{io}. With increasing ionomer content, a growing part of these pores is filled until 100% impregnation of the valid pores is reached.
3. In case the ionomer content exceeds the volume that would suffice for complete impregnation of the outer surface and pores larger than $d_{io,\min}$ with a film of that same thickness, the model solves for the value $r_{p,cut} = d_{io} > d_{io,\min}$ that satisfies the condition that the support surface and all pores larger than $r_{p,cut}$ be impregnated with a film of constant thickness d_{io}. Figure 1 illustrates the possible cases of ionomer filling schematically. In case 3, the increased film thickness and, subsequently, the larger cutoff radius have the effect that more pores are excluded from ionomer impregnation as compared to lower ionomer contents. Consequently, the overall amount of carbon and Pt surface which is covered by ionomer increases with increasing I/C ratio in cases 1 and 2, but the inner ionomer coverage is reduced again in CCLs with sufficiently high ionomer content to trigger case 3. Also, the accessible nanopore volume decreases much more dramatically when pores are cut off by ionomer (case 3) as opposed to merely being slowly filled with ionomer (case 2). It should be noted that the total ionomer loading determines in which qualitative case a CCL is, and the different configurations correspond to different CCL entities. An individual CCL cannot e.g. transit from case 2 to 3 with a sudden reversion of pore impregnation. Besides being adapted from reference,[2] the proposed qualitative behavior concurs with the observations of Andersen et al.[13] who suggested a distinct change in ionomer structure toward aggregation at high ionomer contents. The overall ionomer coverage on Pt consequently increased with ionomer content when the weight percentage was low, but decreased at higher-than-optimum ionomer contents. The proposed increase in ionomer film thickness, either proportional to the I/C ratio[10,14] or only at high ionomer contents[11] is likewise supported by experimental findings. We will show below that further aspects observed in literature, such as no change in ionomer coverage with (low) I/C ratio[11,12] or constant film thickness in certain conditions do not necessarily contradict these assumptions, but can actually be predicted by the proposed model depending on the combination of support morphology, catalyst particle distribution and ionomer content.

In the remainder of this Section, we illustrate how parameters which quantify the ionomer distribution are calculated for the different impregnation cases. At full coverage, the ionomer volume on the outer support surface can be estimated as

$$V_{io,outer,\max}(d_{io}, r_{p,cut}) = \frac{4}{3}\pi N_C((r_C + d_{io})^3 - r_C^3) - d_{io}\int_{r_{p,cut}}^{\infty} A_{p,opening}(\hat{r}_p - d_{io}) n'_{p,Pt/C}(\hat{r}_p)\mathrm{d}\hat{r}_p \quad [28]$$

where

$$n'_{p,Pt/C}(r_p) = v'_{p,Pt/C}(r_p)/V_p(r_p) \quad [29]$$

is the number of pores remaining after Pt loading. The first term in Eq. 28 describes a homogenous ionomer film of thickness d_{io} around a carbon primary particle.[29] As illustrated in Fig. 1a, this film is interrupted above all nanopores that have an opening radius larger than $r_{p,cut} = d_{io}$, i.e. which can potentially be impregnated by ionomer if sufficient ionomer loading is available. For simplification, we assume that the gaps in the otherwise continous ionomer film above these pores can be approximated as disc-like shapes. The overall contribution of these discs is described by the second term in Eq. 28. We distinguish between d_{io} and $r_{p,cut}$ in the given Eqs. since these quantities can generally be set to different values, although we consider them to be equal in our model setup to reduce experimentally unaccessible degrees of freedom.

Note that calculating $n'_{p,Pt/C}$ from $v'_{p,Pt/C}$ as in Eq. 29 implies that we consider the nanopores to still be of cylindrical shape after Pt loading and to approximately have retained their radius-specific volume $V_p(r_p)$. Any losses in $v'_{p,Pt/C}(r_p)$ compared to $v'_{p,C}(r_p)$ are taken to be caused by a decreased number of pores of size class r_p, rather than a changed pore volume. It is likely that both these processes have some influence on experimental PVDs, but they cannot be distinguished without further measurements. However,

particle size distributions measured in literature[1,2] suggest that the inner Pt volume is small compared to the total nanopore volume and thus insufficient to account for the losses in pore volume usually observed. It is more probable that inner or outer Pt blocks the pore entrances,[1,8] thereby reducing the number of accessible pores, but not significantly changing the shape and volume of pores that remain accessible which is why we deem Eq. 29 valid.

To determine the appropriate impregnation case, next to $V_{io,outer,\max}$, we need the maximum ionomer volume that can theoretically be stored within the nanopores of a given Pt/C for a certain film thickness. We consider a fully impregnated pore to be covered in a film of thickness d_{io} along the pore walls and bottom, see Fig. 1c. The corresponding ionomer volume in an individual pore is then composed of a cylinder mantle and a disc at the pore bottom, both with thickness d_{io}, which is expressed as

$$V_{io,p,\max}(r_p, d_{io}) = (\pi r_p^2 d_{io} + (l_p - d_{io}) \times (\pi r_p^2 - \pi (r_p - d_{io})^2)) \quad [30]$$

In most cases, this is the maximum ionomer content that can be located in a pore of size class $r_p > r_{p,cut}$ under the assumption of cylindrical pores and uniform film thickness. However, the deposition of Pt in the pores can in principle cause the remaining available pore volume after Pt loading to be smaller than $V_{io,p,\max}$. We take this into account by comparing the differential volumes $v'_{p,Pt/C}(r_p)$ and $n'_{p,Pt/C}(r_p) V_{io,p,\max}(r_p, d_{io})$ and choosing the smaller value for each pore size class. Expressed as a distribution, the maximum ionomer volume that can be stored in the pores in this way is

$$v'_{io,p,\max}(r_p, d_{io}, r_{p,cut}) = \begin{cases} 0 & \text{if } r_p < r_{p,cut} \\ \min\left(v'_{p,Pt/C}(r_p);\ n'_{p,Pt/C}(r_p) V_{io,p,\max}(r_p, d_{io})\right) & \text{otherwise} \end{cases} \quad [31]$$

and the maximum total ionomer volume within the support nanopores is

$$V_{io,inner,\max}(d_{io}, r_{p,cut}) = \int_0^\infty v'_{io,p,\max}(\hat{r}_p, d_{io}, r_{p,cut}) \mathrm{d}\hat{r}_p \quad [32]$$

For a given Pt/C combination and minimum film thickness, we abbreviate two characteristic volumes $V_{io,1} = V_{io,outer,\max}(d_{io,\min}, d_{io,\min})$ and $V_{io,2} = V_{io,inner,\max}(d_{io,\min}, d_{io,\min})$. The impregnation case is determined by comparing the available ionomer volume $V_{io,total}$ with these quantities:

1. For $V_{io,total} \leqslant V_{io,1}$, all ionomer volume is located on the support surface such that $V_{io,outer} = V_{io,total}$ and $V_{io,inner} = 0$. We assume that the ionomer film cannot become arbitrarily thin but, due to surface tension, rather forms islands which exhibit the set minimum thickness $d_{io} = d_{io,\min}$. The overall coverage of the available support surface can hence be smaller than unity (Fig. 1a).
2. For $V_{io,1} < V_{io,total} \leqslant V_{io,1} + V_{io,2}$, there is full coverage with the minimum film thickness on the outer support surface such that

Table I. Morphological parameters of investigated CCLs from experimental and simulated data at an I/C ratio of 0.7. Parameters with only one value are the same for simulation and experiment.

Carbon support (exp/sim)	Unit	CB	GCB	V1	K4	K8	K13
Nanopore volume	$cm^3 g_C^{-1}$	0.57	0.16	0.09	0.23	0.48	1.05
Specific surface area	$m^2 g_C^{-1}$	875 / 997	164 / 364	141 / 293	382 / 471	778 / 762	1335 / 1216
Primary particle porosity $x_{C,p}$	%	—/ 36.3	—/ 13.8	—/ 8.3	—/ 18.7	—/ 32.4	—/ 51.2
Pt/C (exp/sim)	Unit	CB	GCB	V1	K4	K8	K13
Nanopore volume	$cm^3 g_C^{-1}$	0.34 / 0.46	0.14 / 0.15	0.07 / 0.07	0.20 / 0.19	0.42 / 0.29	0.88 / 0.82
Specific surface area	$m^2 g_C^{-1}$	477 /—	137 /—	128 /—	320 /—	677 /—	1235 / —
Inner Pt particle radius	nm	1.15 ± 0.25	1.45 ± 0.25	1.2 ± 0.15	1.2 ± 0.15	1.15 ± 0.15	1.1 ± 0.15
Outer Pt particle radius	nm	1.4 ± 0.25	1.65 ± 0.25	1.7 ± 0.3	1.6 ± 0.8	1.4 ± 0.25	1.4 ± 0.2
Inner Pt particle frequency	%	62	5	13	25	64	73
Outer Pt particle frequency	%	38	95	87	75	36	27
Inner ECSA	$m^2 g_{Pt}^{-1}$	62	4	6	14	60	72
Outer ECSA	$m^2 g_{Pt}^{-1}$	38	68	78	77	50	43
Pt/C/ionomer (exp/sim)	Unit	CB	GCB	V1	K4	K8	K13
Nanopore volume	$cm^3 g_C^{-1}$	0.14 / 0.028	0.04 / 0.011	—/ 0.003	—/ 0.011	—/ 0.055	—/ 0.65
Specific surface area	$m^2 g_C^{-1}$	205 /—	51/—	—/—	—/—	—/—	—/—
Ionomer coverage outer Pt	—	—/ 1.0	—/ 1.0	—/ 1.0	—/ 1.0	—/ 1.0	—/ 1.0
Avg. ionomer coverage inner Pt	—	—/ 0.88	—/ 0.82	—/ 0.56	—/ 0.68	—/ 1.0	—/ 0.32
Partition ionomer in pores	%	—/ 22.1	—/ 12.0	—/ 5.8	—/ 17.6	—/ 38.2	—/ 28.1
Cut—off radius	nm	—/ 1.38	—/ 2.02	—/ 2.27	—/ 1.81	—/ 1.18	—/ 1.0
Secondary pore volume in CCL	%	—/ 34.8	—/ 34.8	—/ 34.8	—/ 34.8	—/ 34.8	—/ 34.8
Pore volume occupied by Pt/io	%	—/ 25.2	—/ 46.2	—/ 41.1	—/ 48.0	—/ 51.6	17.9
Materials (exp/sim)	Unit	CB	GCB	V1	K4	K8	K13
d_{ccl}	μm	—/ 5.40	—/ 3.63	—/ 8.40	—/ 9.47	—/ 11.40	—/ 15.79
A_{ccl}	cm^2	29.2	29.2	36.0	36.0	36.0	36.0
L_{Pt}	mg cm^{-2}	0.051	0.048	0.19	0.19	0.19	0.19
$wt\%_{Pt/cat}$	%	28.6	29.3	40.0	40.0	40.0	40.0
$wt\%_{io}$	%	33.3	33.1	29.6	29.6	29.6	29.6
I/C	—	0.7	0.7	0.7	0.7	0.7	0.7

$V_{io,outer} = V_{io,1}$. Pores with openings larger than $r_{p,cut} = d_{io,\min}$ can now become partially impregnated with ionomer, the degree of coverage depending on the available inner ionomer volume $V_{io,inner} = V_{io,total} - V_{io,outer}$ (Fig. 1b).

3. For $V_{io,total} > V_{io,1} + V_{io,2}$, all pores larger than the cutoff radius are 100% impregnated. In order to use all available ionomer and still fulfill the condition that the cutoff radius be the same value as the film thickness, the film thickness is adapted to the value $d_{io} = r_{p,cut} > d_{io,\min}$ which satisfies the condition

$$V_{io,outer,\max}(d_{io}, d_{io}) + V_{io,inner,\max}(d_{io}, d_{io}) = V_{io,total} \quad [33]$$

with ionomer volumes $V_{io,inner} = V_{io,inner,\max}(d_{io}, d_{io})$ and $V_{io,outer} = V_{io,outer,\max}(d_{io}, d_{io})$ (Fig. 1c).

The distribution behavior of ionomer within the porous CCL is thus fully determined by the given ionomer content, the minimum thickness of the formed ionomer film, the carbon primary particle size, the nanopore distribution and the distribution of Pt within the pores. Lastly, we use the derived quantities to give a mathematical description of the Pt/ionomer interface. For Pt located on the outer support surface, the coverage with ionomer is independent of the particle size. An individual particle can either be covered or not covered by ionomer, but the statistical coverage of all particles in a size class equals the coverage found on the outer surface

$$\Theta_{io/Pt,outer} = \frac{V_{io,outer}}{V_{io,outer,\max}(d_{io}, r_{p,cut})} \quad [34]$$

For Pt particles located in nanopores, the case is different. Particles situated in pores below the cutoff radius are never contacted by ionomer while the statistical coverage on particles in pores above the cutoff radius corresponds to the percentage to which the pore is impregnated (Fig. 1b). In order to find a general expression for the ionomer coverage on inner particles of a size class r_{Pt}, we therefore need information on how many particles of that size class are located in pores that are contacted by ionomer. This information is provided by the previously introduced distribution $n''_{Pt,p}(r_{Pt}, r_p)$ and we can derive

$$\Theta_{io/Pt,inner}(r_{Pt}, d_{io}, r_{p,cut}) = \frac{V_{io,inner}}{V_{io,inner,\max}(d_{io}, r_{p,cut})} \times \frac{\int_{r_{p,cut}}^{\infty} n''_{Pt,p}(r_{Pt}, \hat{r}_p)\mathrm{d}\hat{r}_p}{n'_{Pt,inner}(r_{Pt})} \quad [35]$$

where the second fraction expresses the partition of inner Pt particles of size r_{Pt} sitting in impregnated pores. In summary, for a morphological description of the CCL, the model requires the material composition, pore and particle size distributions, partition of particles inside pores and assumptions on carbon primary particle size, basic pore morphology and minimum ionomer film thickness. We will show that this information, in our case obtained from

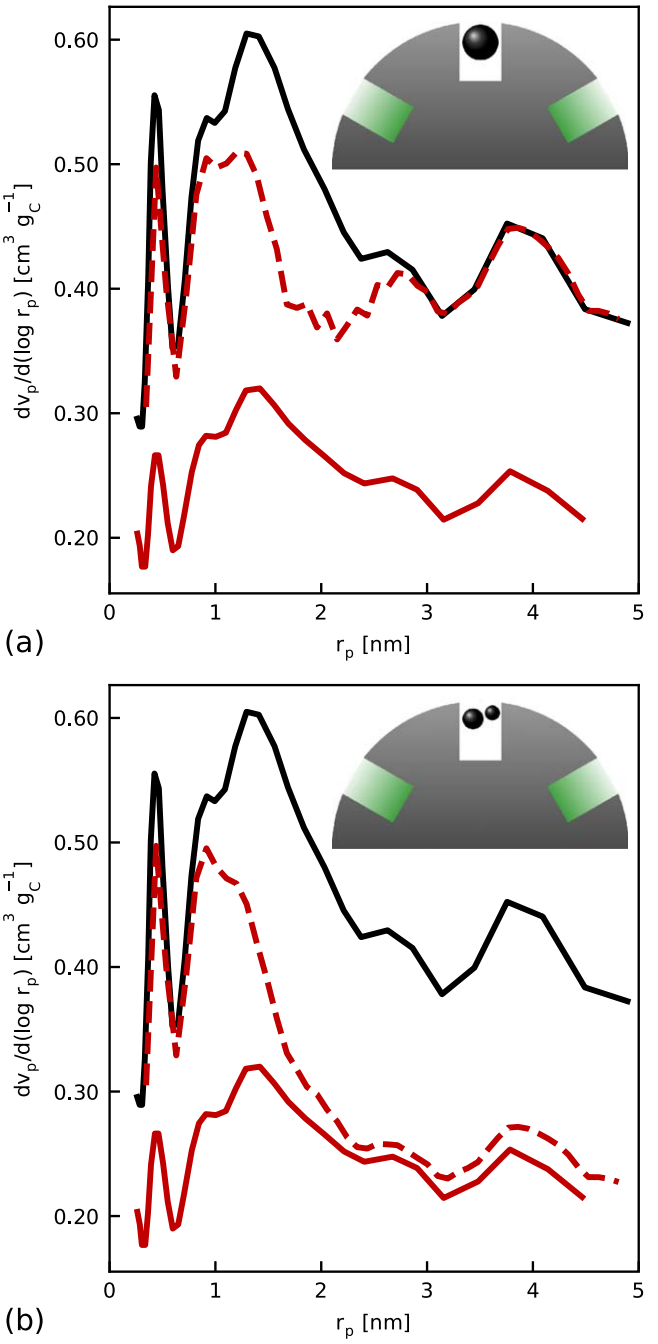

Figure 2. Measured PVDs of CB before loading (solid black) and after Pt loading (solid red), obtained from Ref. 1. Corresponding simulations for different scenarios of Pt deposition (a) using Eq. 36; (b) using Eq. 38. Green areas in inset schematics indicate accessible pore volume after Pt loading.

Table II. Set model parameters which are the same for every investigated CCL.

Parameter	Unit	Set model value
Carbon density ρ_C	g cm^{-3}	1.0
Pt density ρ_{Pt}	g cm^{-3}	21.45
Ionomer density ρ_{io}	g cm^{-3}	1.15
Carbon primary particle radius r_C	nm	15
Pore depth l_p	nm	10
Primary particle packing density x_{pack}	—	0.37
Minimum outer ionomer film thickness $d_{io,\min}$	nm	1.0

literature, is sufficient to reproduce various measurement methods with good qualitative and quantitative correspondence.

Results and Discussion

We present simulation results for six exemplary combinations of a Pt catalyst and porous carbon support which we adopted from literature. The data were taken from the works of Park and co-workers[1] and Kobayashi and co-workers,[2] hereafter also denoted as reference publications. Both works provide extensive measurement data on a variety of supports before and after loading with Pt and ionomer, respectively. From Ref. 2, two of the presented Pt/support combinations were adopted, namely Pt on highly porous Ketjenblack (Pt/CB) and Pt on graphitized Ketjenblack (Pt/GCB). All four Pt/support combinations presented in Ref. 2 were adopted, namely, one with Pt on Vulcan (Pt/V1) and three with Pt on Ketjenblack with ascending porosity (Pt/K4, Pt/K8, Pt/K13). We first focus on the model representation of porous supports and their loading with Pt catalyst. Next, we present simulation results for support impregnation with ionomer and the subsequent properties of the Pt/ionomer interface within the simulated catalyst layers. Finally, we exemplify how the model framework can be modified to represent measured results more accurately in case suitable data are available. Measured and simulated properties of the individual catalyst layers are summarized in Table I. Additional model parameters which apply to all supports are given in Table II.

Pt distribution on porous carbon supports.—First, the log-differential PVDs extracted from the reference publications were transferred to the corresponding differential distributions v'_p.[30] Under the assumption of cylindrical pores, the pore size distributions n'_p were then obtained. The inner and outer Pt particle size distributions were assumed to be Gaussian distributions with mean particle radius and standard deviation corresponding to the values obtained from STEM data in the reference publications. By normalizing the particle size distributions as described above, it was ensured that they corresponded to the Pt loading as well as the percentage of Pt particles in the nanopores and on the support surface that were reported in the reference publications. From the particle and pore size distributions, the distribution of Pt in the nanopores $n''_{Pt,p}$ was calculated. Concurrent with the reference publications, we consider nanopores to denote pores with $r_p \leqslant 5$ nm.

With the basic distributions given, we sought to calculate the PVD after Pt loading $v'_{p,Pt/C}$ which is a quantity that can be directly compared to literature. As an example for our considerations, we use Pt/CB which has an intermediate surface area and exhibits nanopores in the whole observed size range from 0.25 to 5 nm pore radius. In the experiment, Pt loading decreased the accessible nanopore volume by about 40% for this support. As stated before, this cannot be explained purely by the comparatively small additional Pt volume, but is rather attributed to Pt blocking the nanopore entrances[1,8] with subsequent loss of the full nanopore volume below and hence a reduction in the number of pores. We used the model to explore how this process could work in a qualitative way.

The first case we investigated was the assumption that a Pt particle whose size is close to that of the pore in which it is lodged is sufficient to block the pore. With the previously obtained distribution $n''_{Pt,p}$, the number of Pt particles whose radius is 60% or more of the radius of their pore can be calculated. Assuming that each of these particles blocks an entire pore, the fraction of blocked pores is

$$x_{p,Pt/C,blocked}(r_p) = \frac{\int_{0.6r_p}^{r_p} n''_{Pt,p}(\hat{r}_{Pt}, r_p)\mathrm{d}\hat{r}_{Pt}}{n'_{p,C}(r_p)} \quad [36]$$

and the remaining nanopore volume distribution after Pt loading is

$$v'_{p,Pt/C}(r_p) = (1 - x_{p,Pt/C,blocked}(r_p))v'_{p,C}(r_p) \quad [37]$$

Figure 2a shows the resultant PVD compared to the data measured in Ref. 1. For better comparison to literature, all PVDs in this work are plotted in the log-differential form.[30] Clearly, the simulated distribution fails to capture the qualitative behavior of the experimental one. The nanopore volume is reduced between 0.5 and 2.5 nm which

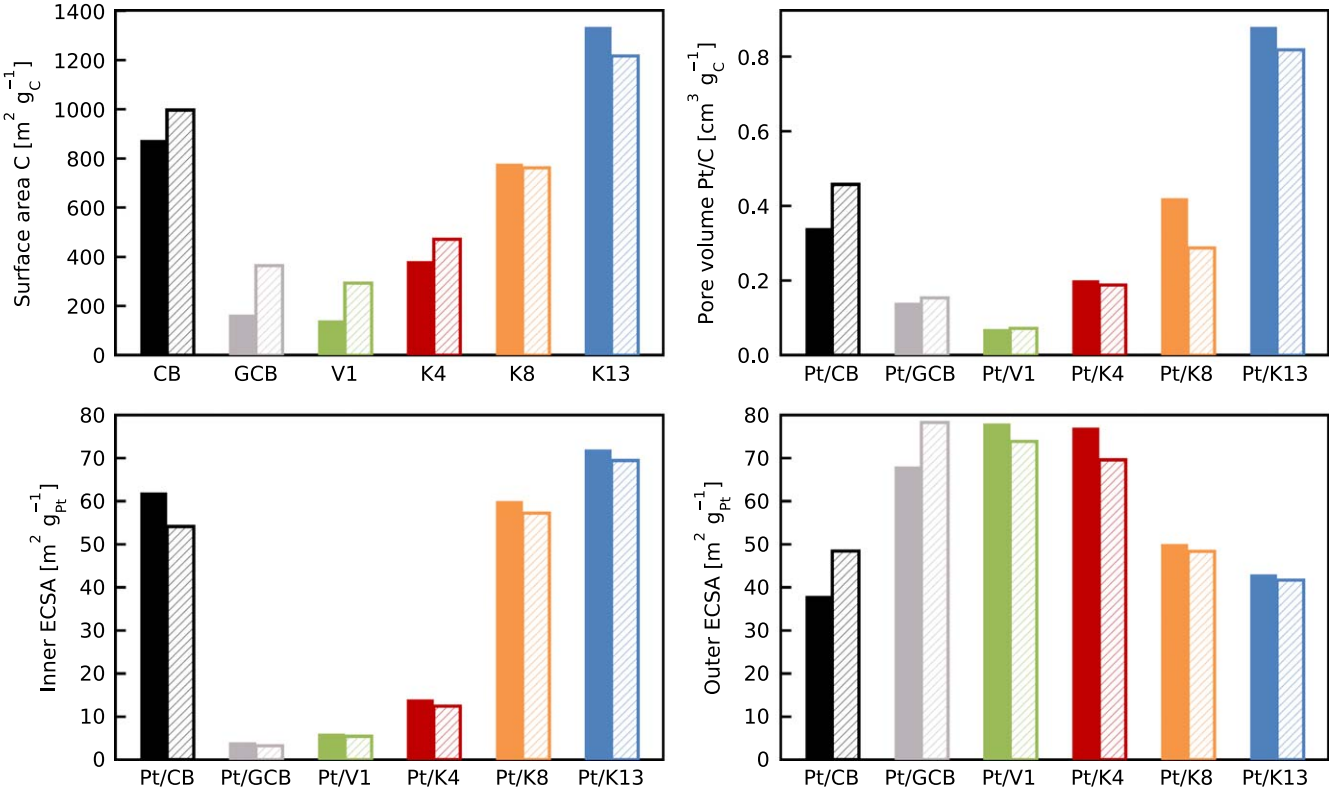

Figure 3. Comparison between experimental (solid) and simulated (hatched) properties of the six catalyst and support combinations.

is the size range corresponding to that of the inner Pt particles ($r_{Pt} = 1.15 \pm 0.25$ nm, see Table I). Larger pores are unaffected because the radii of the Pt particles stored in the pores do not amount to the 60% of the pore radius we assumed as a criterion for blockage. Smaller pores are likewise unaffected because Pt particles are generally too large to be stored in these pores. However, the experimental data suggests nanopore volume loss in all pore size ranges. Therefore, we considered a different scenario where the cross-section of all particles sitting inside the pores of a size class was compared to the pore opening surface area. We assumed that nanoparticles can effectively block an area twice that of their collective cross-sections, hence, in this scenario, the fraction of blocked pores is approximated as

$$x_{p,Pt/C,blocked}(r_p) = \frac{2\int_0^\infty \pi \hat{r}_{Pt}^2 n''(\hat{r}_{Pt}, r_p)\mathrm{d}\hat{r}_{Pt}}{A_{p,opening}(r_p)n'_{p,C}(r_p)} \quad [38]$$

In this scenario, it is possible for several small particles to block a pore as opposed to necessitating one large particle with a radius close to the pore size. Note that the model does not distiguish where in the nanopore or in which particular nanopores of a given size class the particles sit. It has been suggested that Pt deposition preferentially occurs near the entrance of a pore due to the higher reactivity of edge sites,[8] hence, we consider the statistically expressed partition of blocked pores in Eq. 38 reasonable. The resultant PVD is again calculated according to Eq. 37 and is shown in Fig. 2b. For pores larger than 1.5 nm, the model now captures the experimental data very well, but the predicted volume loss for smaller pores is still insufficient. It is likely that additional factors contributed to the measured volume loss, but deriving their nature from the data was not straightforward. An obvious possibility is the blockage of pores due to outer Pt. However, in the case of Pt/CB, the accumulated cross-sections of all outer Pt particles only amount to about 14% of the surface area constituted by the openings of pores smaller than $r_p = 1.5$ nm. Even if every outer Pt particle sat on the entrance of one or several of these pores, losses would not be sufficiently high due to the vast number of small pores in the given sample. Since we have no information on the Pt deposition method of this commercial catalyst, we can only speculate that the smallest pores are potentially more vulnerable to blockage during the process, possibly by small Pt particles which may have been unresolved in STEM measurements or by carbon fragments or neighbouring primary particles. In addition, calculating pore volumes in adsorbents that feature both pores below a radius of 1 nm and larger pores is challenging due to the concurrent processes of micropore filling and monolayer-multilayer adsorption in such materials.[8,31] This was addressed in reference publication[1] by using quenched solid density functional theory analysis to calculate the PVDs, but it is possible that small pore sizes are associated with a higher measurement uncertainty. For the purposes of modeling Pt deposition, we remain with the second scenario in the following. The proposed mechanism showed the best match for the five other supports and reasonable accordance with the larger pores of Pt/CB. The experimental and simulated PVDs after Pt deposition for all six supports can be found in the next Section in Fig. 4, together with the distributions of the unloaded support and after ionomer addition.

We conclude our considerations on loading porous supports with Pt by comparing characteristics of the simulated CCLs, calculated from the described pore and particle size and volume distributions, to experimental data. Figure 3 shows the support surface area, the total nanopore volume after Pt addition and the ECSA of the inner and outer Pt. For calculating the support surface area, we only took into account the contribution of pores with $r_p \geqslant 0.5$ nm to approximate the limit[31] of the nitrogen adsorption based BET surface area measurements performed in the reference publications. This only affects Pt/CB and Pt/GCB as the characterized pore size range for the other supports starts at 1 nm. Generally, the depicted integral quantities match the experimental data well, suggesting that our assumptions on basic pore morphology and catalyst distribution on

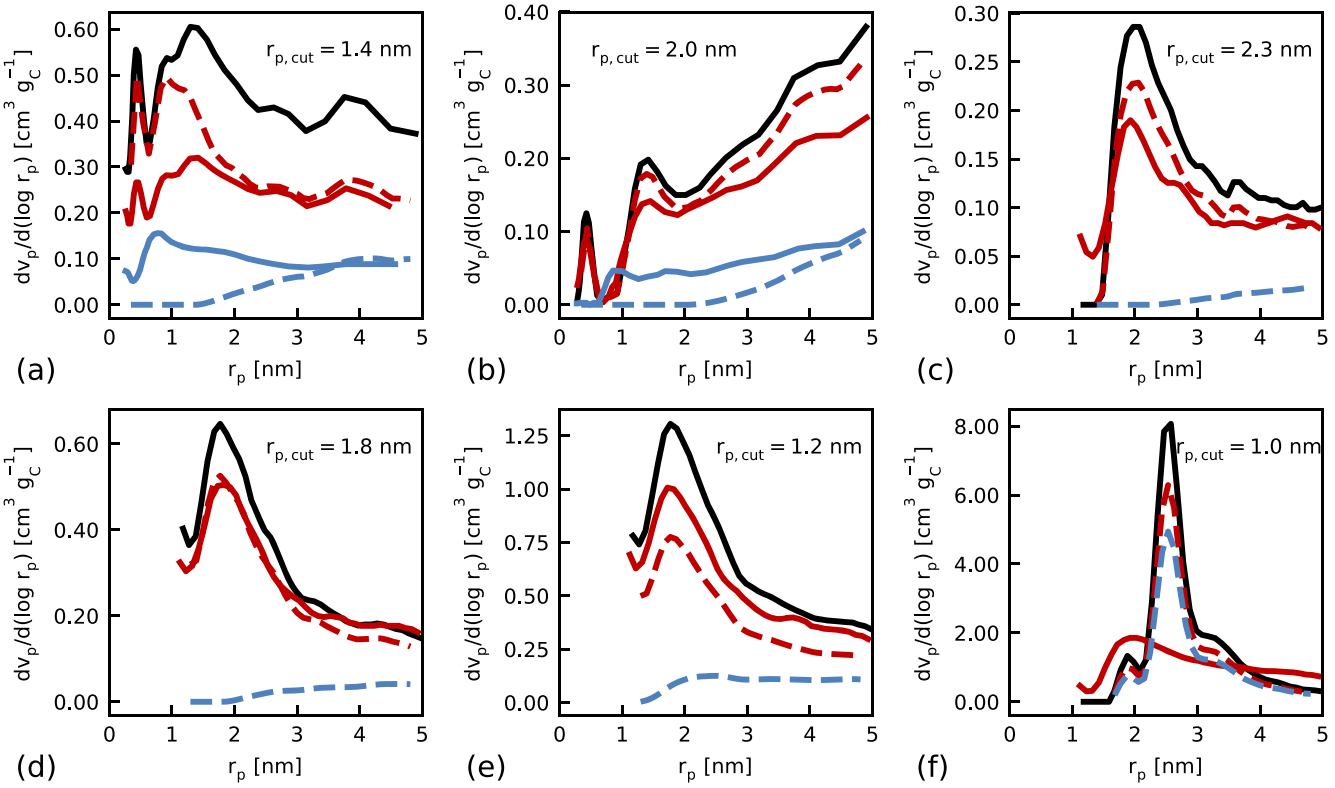

Figure 4. Measured PVDs of (a) CB; (b) GCB; (c) V1; (d) K4; (e) K8 and (f) K13 before loading (solid black), after Pt loading (solid red) and after ionomer loading (solid blue, data only available for CB and GCB), obtained from Refs.1,2. Corresponding simulations after Pt loading (dashed red line) and ionomer loading (dashed blue line).

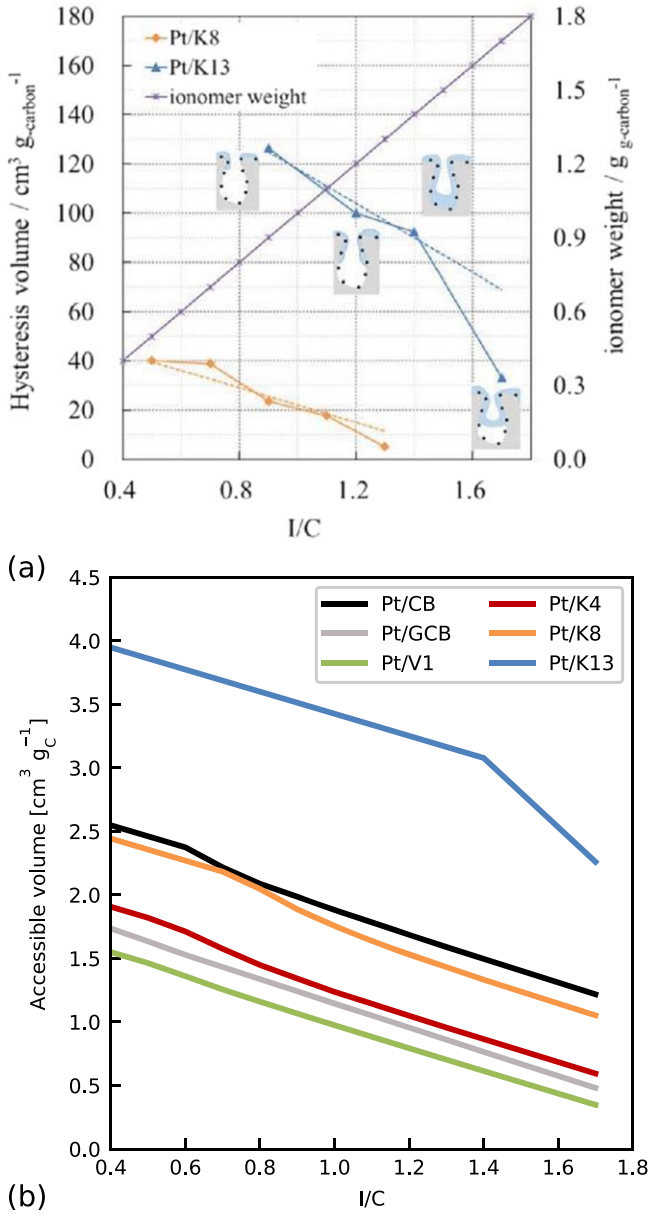

Figure 5. Accessible pore volume for different I/C ratios (a) measured with N_2 adsorption in the reference publication[2]; (b) simulated using Eq. 41. Figure (a) was reprinted with permission from https://pubs.acs.org/doi/abs/10.1021/acsaem.0c02841. Further permission related to this Fig. should be directed to the American Chemical Society ACS.

the support are reasonable when large numbers are involved, even though representing an individual pore by a cylinder may seem a strong simplification. A notable fact in Fig. 3 is that the relative deviation of the calculated support surface area is highest for the least porous supports, GCB and V1. It is likely that these are not represented well by cylindrical pores of uniform length l_p. Presumably, nanopore morphology is closer to a semi-sphere in these support types [1]. At the same opening radius and volume, the specific surface area of a semi-spherical pore is less than that of a cylindrical pore which would explain why the model overestimates the surface area in these cases. By replacing Eqs. 11 to 13, a different representation of basic pore morphology can easily be formulated into the model in case corresponding information on the support is available. The data shown in Fig. 3 is also summarized in Table I.

Support impregnation with ionomer.—With correspondence of the simulated and experimental Pt/C combinations established, we next focused on the effects of adding ionomer to the catalyst and support. An I/C ratio of 0.7 was set for correspondence with the reference work[1] where pore volume distributions after both Pt and ionomer loading are provided. A minimum ionomer film thickness of $d_{io,\min} = 1$ nm was chosen for all support types. This value is in accordance with the findings of Park et al.[1] who reported a uniform and continous ionomer film of 1–2 nm thickness on Pt/CB. However, they also observed that the film tended to be less uniform and more concentrated near Pt particles with increased degree of graphitization of the support. This was not taken into account in the model, but is discussed in the context of the Pt/ionomer interface in the next Section.

With the total ionomer volume $V_{io,total}$ and minimum film thickness $d_{io,\min}$ given, the inner and outer ionomer volumes, the cutoff radius and the actual film thickness were calculated as described above. Using these quantities, the remaining PVD after ionomer impregnation for each support was calculated as

$$v'_{p,Pt/C/io}(r_p, d_{io}, r_{p,cut}) = \begin{cases} v'_{p,Pt/C}(r_p) - \dfrac{V_{io,outer}}{V_{io,outer,\max}(d_{io}, r_{p,cut})} v'_{p,Pt/C}(r_p) & for\ r_p \leqslant r_{p,cut} \\ v'_{p,Pt/C}(r_p) - \dfrac{V_{io,inner}}{V_{io,inner,\max}(d_{io}, r_{p,cut})} v'_{io,p,\max}(r_p, d_{io}, r_{p,cut}) & otherwise \end{cases} \quad [39]$$

The first case accounts for the fact that, at very low ionomer contents, the available ionomer volume may not be sufficient to cover all support surface and pore openings smaller than $r_{p,cut}$ in a film of thickness $d_{io,\min}$. In this case, on average, only a percentage equal to $V_{io,outer}/V_{io,outer,\max}(d_{io}, r_{p,cut})$ of these pores is cut off with their respective pore volumes being subtracted from the overall remaining pore volume. If the ionomer content is high enough to achieve full outer coverage, there is no contribution to the pore volume from the pores smaller than $r_{p,cut}$ anymore. In the second case of pores larger than $r_{p,cut}$, the volume of a pore with size r_p is diminished by the ionomer volume stored in that pore.

Figure 4 shows the simulated PVDs of the carbon support before and after loading with Pt and ionomer in comparison with the experimental data. Note that measured PVDs after ionomer addition are only available for Pt/CB and Pt/GCB since the reference publication[2] did not feature this data. After the addition of ionomer, the remaining nanopore volume is significantly reduced. For all supports except Pt/K13, the calculated ionomer film thickness and cutoff radius are larger than the set minimum film thickness, meaning that ionomer impregnation case 3 prevails at I/C = 0.7. The available ionomer volume is more than the volume theoretically needed to cover the outer support surface and all pores with $r_p > d_{io,\min} = 1$ nm in a film of that same thickness. Consequently, the model solves for a larger value $d_{io} = r_{p,cut}$ at which all ionomer can be stored in the CCL, with any pores above the cutoff radius being fully impregnated (compare to Fig. 1c). The calculated cutoff radius depends on the support morphology and tends to be smaller for supports with high nanopore volume. For these, more ionomer can be stored in the pores and case 3 is only triggered at comparatively high ionomer contents. However, for instance, Pt/K8 has a smaller cutoff radius than Pt/CB despite the pore volume of the latter being larger. This is due to the fact that a large contribution to nanopore volume comes from small pores <1 nm in Pt/CB. For a set minimum film thickness of 1 nm, these pores are always cut off and no ionomer can be stored inside. Contrary to the other supports, Pt/K13, with the highest specific surface area and nanopore volume, is in case 2, with the cutoff radius still at $r_{p,cut} = d_{io,\min}$. The ionomer volume is sufficient to reach full outer coverage and enter the nanopores, reducing the nanopore volume, but not enough for 100% impregnation of pores >1 nm. While this is plausible, it must be noted that the simulated PVD after Pt deposition, which in turn influences the PVD after ionomer loading, deviates significantly

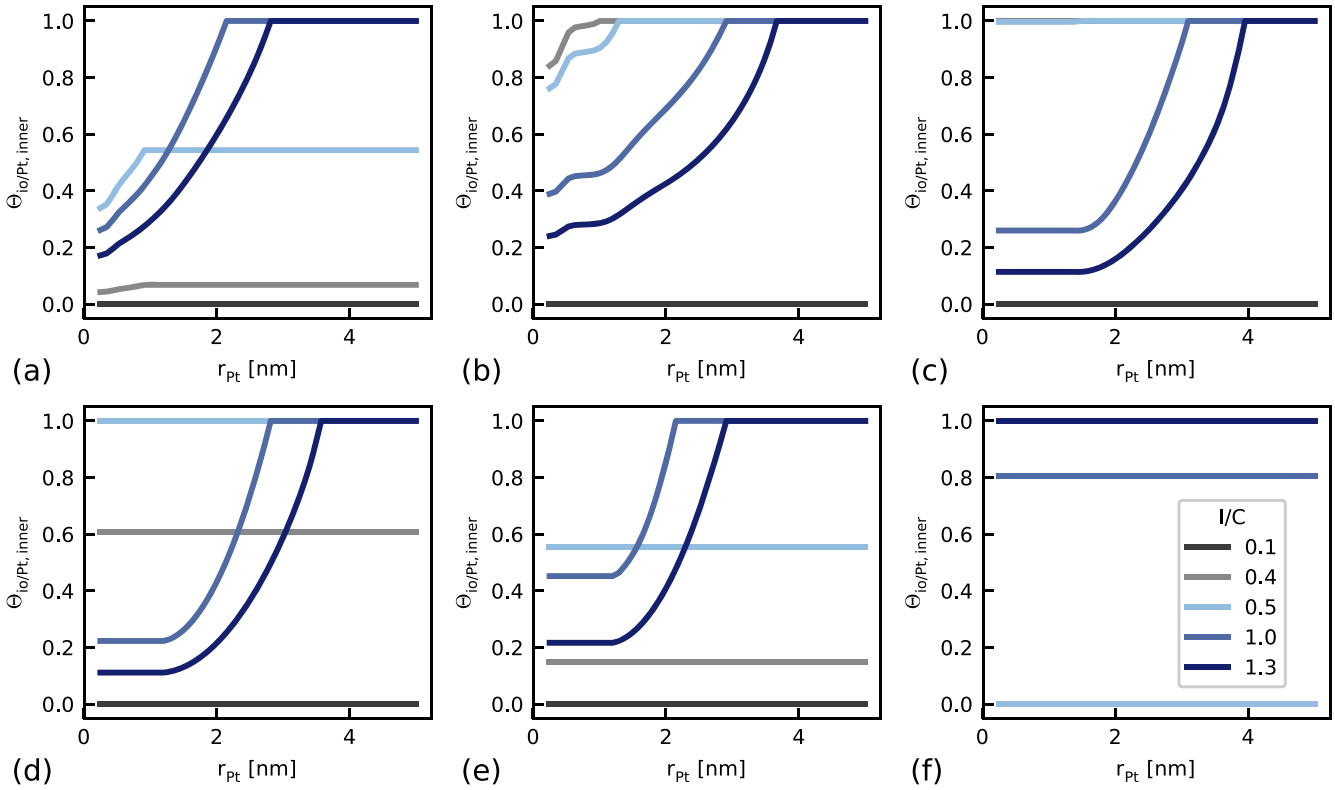

Figure 6. Ionomer coverage on inner Pt particles with respect to particle size class for (a) Pt/CB; (b) Pt/GCB; (c) Pt/V1; (d) Pt/K4; (e) Pt/K8 and (f) Pt/K13. The legend in (f) refers to all subfigures.

from the measured data for Pt/K13 because pore volume gain in certain size classes cannot be emulated by the model. For CB and GCB, we exemplify in the last Section of the results part how the model can be adapted to capture the available validation data better.

In order to compare our model to further data, we performed simulations corresponding to measurements in the reference publication of Kobayashi et al.[2] The authors did not provide pore volume distributions after ionomer loading, however, they ran N_2 adsorption measurements for varying I/C ratios to obtain the adsorption/desorption hysteresis volume from which they derived the status of pore impregnation. In order to generate comparable data, we used our model to calculate the accessible volume within the CCL at different I/C ratios. As accessible volume, we consider the secondary pore space between carbon primary particles plus the nanopore volume which is not taken up or blocked by ionomer. With a given ionomer volume and corresponding impregnation case, the secondary pore volume is calculated as

$$V_{ccl,secondary} = V_{ccl} - V_{io,outer} - V_{Pt,outer} - V_{C,total} \quad [40]$$

The accessible volume is then calculated by adding the cumulative contribution of the nanopores after ionomer loading

$$V_{ccl,accessible} = V_{ccl,secondary} + \int_0^{\infty} v'_{p,Pt/C/io}(\hat{r}_p, d_{io}, r_{p,cut})\mathrm{d}\hat{r}_p \quad [41]$$

Figure 5 shows the reference data and simulated accessible volume in the CCL for I/C ratios between 0.2 and 1.7. The curves of the more porous supports (Pt/CB, Pt/K4, Pt/K8, Pt/K13) exhibit inflection points where the slope of the curve changes to a steeper decrease and then, for Pt/CB, Pt/K4 and Pt/K8, back to the initial slope. These points mark the transition between different ionomer impregnation cases. At low ionomer contents, in cases 1 and 2, any additional ionomer volume reduces the accessible pore volume by an equal amount (Figs. 1a and 1b). However, at higher ionomer contents in case 3, d_{io} and $r_{p,cut}$ increase, cutting off more nanopores than at lower I/C ratios and resulting in more drastic loss of accessible volume (Fig. 1c). Once $r_{p,cut}$ is in size ranges above which there exist only few pores whose blockage hardly impacts the PVD, adding yet more ionomer mainly increases the outer film thickness and the curve reassumes its initial slope. For supports with small overall nanopore volume such as Pt/GCB and Pt/V1, pore impregnation takes place in a very narrow range of I/C values and changes in the curve slope are hardly noticeable.

The qualitative behavior corresponds well to that observed by Kobayashi and co-workers for Pt/K8 and Pt/K13 (Fig. 5a), which is to be expected since their considerations on pore impregnation formed the basis for our model. From a quantitative point of view, the I/C ratios at which the inflection points taken to be related to pore blockage occur also match the experimental data well. The ordinate values cannot be compared directly due to the conversion factor between pore volume and liquid nitrogen volume[7,8] and also because we considered the entire contribution of the secondary pore volume in the model. In the measurement, N_2 adsorption in primary pores is to some extent accompanied by adsorption in larger pores and on the external surface of the primary particles.[8] Since the contributions of these processes cannot be easily distinguished, we considered the simulations to correspond best to the experiment when the offset due to secondary pores was taken into account.

Pt/ionomer interface.—Our considerations regarding ionomer in porous supports so far focused on illustrating in which way nanopores can be blocked or impregnated by ionomer. In this Section, we return to the Pt particles located within the nanopores and on the support surface and the consequences for the protonic accessibility of these particles. Equation 35 was used to calculate the ionomer coverage on the inner Pt particles $\Theta_{io/Pt,inner}$ for various I/C ratios. Note that in this equation, the decision whether a Pt particle

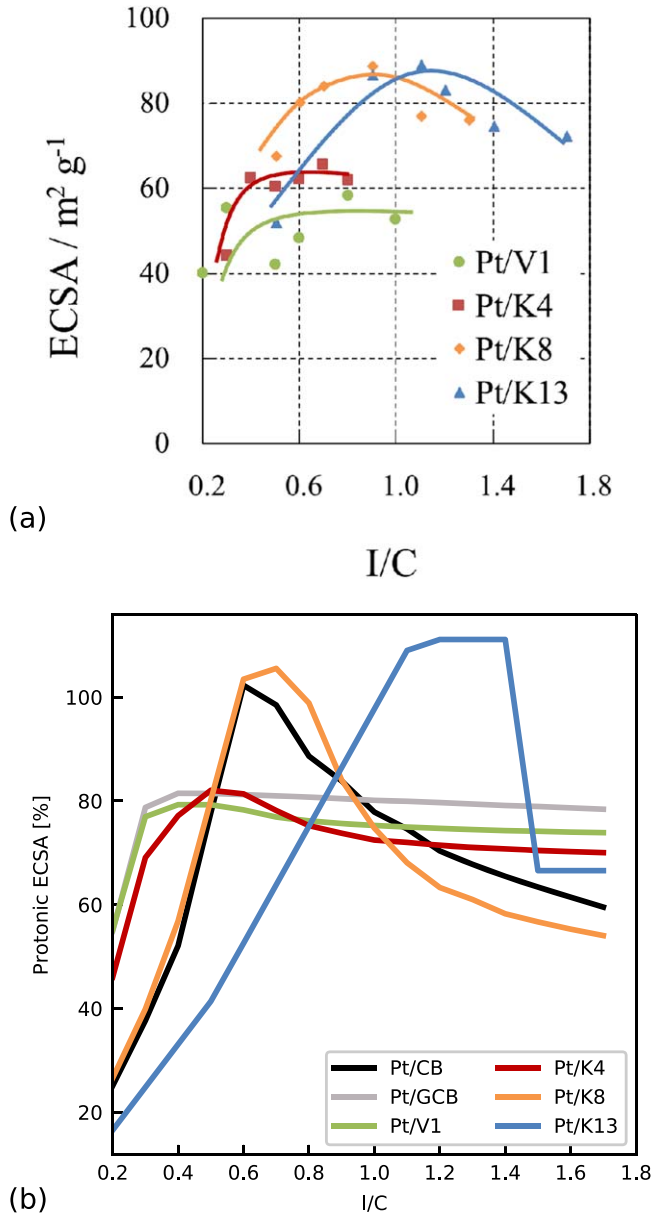

Figure 7. (a) ECSA for different supports and I/C ratios measured in the reference publication;[2] (b) Simulated ECSA of Pt particles contacted by ionomer, calculated using Eq. 42. Figure (a) was reprinted with permission from https://pubs.acs.org/doi/abs/10.1021/acsaem.0c02841. Further permission related to this Fig. should be directed to the American Chemical Society ACS.

can be contacted by ionomer depends on the size of the pore in which the particle sits, but not on whether the pore is considered to be blocked by Pt. One could argue that the statistical portion of Pt which blocks pores should be removed from the pool of particles potentially contacted by ionomer. However, we stated above that Pt blocks the entrance of a pore such that the entire pore is removed from the PVD and does not appear in $n'_{p,Pt/C}$ (compare to inset in Fig. 2b). The consequence is that the outer ionomer film evolves to be continous (i.e. not interrupted) above this pore according to Eq. 28. The particles in turn sitting at the pore entrance, we consider that coverage on these particles is guaranteed by the outer film in this particular case.

Figure 6 shows the ionomer coverage on particles inside pores against the particle size class. At low I/C ratios, in case 1, the coverage on inner particles is zero until full outer coverage has been reached. In case 2, the maximum coverage that can be reached on particles larger than the cutoff radius (and hence in pores larger than the cutoff radius) is $V_{io,inner}/V_{io,inner,\max}(d_{io,\min}, d_{io,\min})$. Smaller particle size classes exhibit coverages smaller than this value due to the fact that some of the particles in the size class can be located in non-impregnated pores below the cutoff radius (Fig. 1a). At the I/C ratio where the maximum $\Theta_{io/Pt,inner}$ first reaches 100%, case 3 commences. The cutoff radius becomes larger, and is discernable in the plots as the radius at which the curve assumes a value of 1. Particles with $r_{Pt} > r_{p,cut}$ are always fully covered with ionomer in case 3 whereas the overall coverage of particles below the cutoff radius actually becomes less since more of the pores they are sitting in are blocked at higher ionomer contents.

The consequence of the predicted behavior is that for each support, there is an I/C ratio where a maximum overall ionomer coverage on Pt is reached before it is reduced again. In many publications,[17,32–35] the existance of such an optimum ionomer content was shown and is usually considered as the balance point between sufficient protonic binding and sufficient remaining accessible volume for gas and water transport. Our findings add a further dimension to this by suggesting that, regardless of reactant transport, also the protonic accessibility of Pt might not grow indefinitely with adding more ionomer but in fact exhibit a maximum at intermediate ionomer contents, a fact that is supported by recent findings of Andersen et al.[13] For a better visualization of this, we used the model to calculate the actual protonically accessible ECSA on each support for different I/C ratios. The contribution of each particle size class was weighted with its respective ionomer coverage, both for inner Pt and outer Pt particles. The coverage on the latter is independent of particle size such that

$$A_{Pt,total,protonic} = \Theta_{io/Pt,outer} A_{Pt,outer} + \int_0^\infty \Theta_{io/Pt,inner}(\hat{r}_{Pt}, d_{io}, r_{p,cut}) \times A_{Pt}(\hat{r}_{Pt}) n'_{Pt,inner}(\hat{r}_{Pt}) \mathrm{d}\hat{r}_{Pt} \quad [42]$$

The obtained ECSA, normalized to the total Pt loading, is shown in Fig. 7 in comparison to ECSA measurements from the reference publication of Kobayashi et al.[2] The modeled results match the experimental data very well. The more porous supports Pt/CB, Pt/K8 and Pt/K13 exhibit distinct maxima around I/C values of 0.8 and 1.2, respectively. For the less porous supports Pt/GCB, Pt/V1 and Pt/K4, the ECSA increases up to an I/C value around 0.5 and then remains mostly constant. The reason is that on these supports, the largest contribution to the ECSA comes from Pt located on the outer support surface. In contrast to the ionomer coverage on inner particles, the coverage on the outer particles always increases with I/C or remains constant which is why there is little change in the ECSA after full outer coverage has been reached. From a quantitative point of view, the model slightly overestimates the ECSA values, particularly for Pt/V1 and Pt/K4. As mentioned in the previous Section, Park et al.[1] noticed in their work that the outer ionomer film tended to be less continous with less porous supports and increased degree of support graphitization. The largest part of the ECSA being located on the surface of Pt/GCB, Pt/V1 and Pt/K4, a discontinous outer ionomer film would therefore significantly reduce the protonically connected ECSA which could explain the discrepancy between simulation and experiment. This could be represented in the model by reducing the aspired maximum outer ionomer coverage proportional to the degree of graphitization of the support.

Finally, we recapitulate that there have been different findings in literature as to whether the ionomer coverage remains constant[12] or changes with I/C[10,11] and whether the ionomer film thickness remains constant[36] or increases.[10,14,15] In the presented simulation results, we can actually find all these aspects. The outer coverage increases in case 1, but stays constant in case 2. The film thickness stays constant in cases 1 and 2, but increases in case 3. Thus, all these processes appear, but when and how depends on the support morphology and material combination. It is likely that the situation

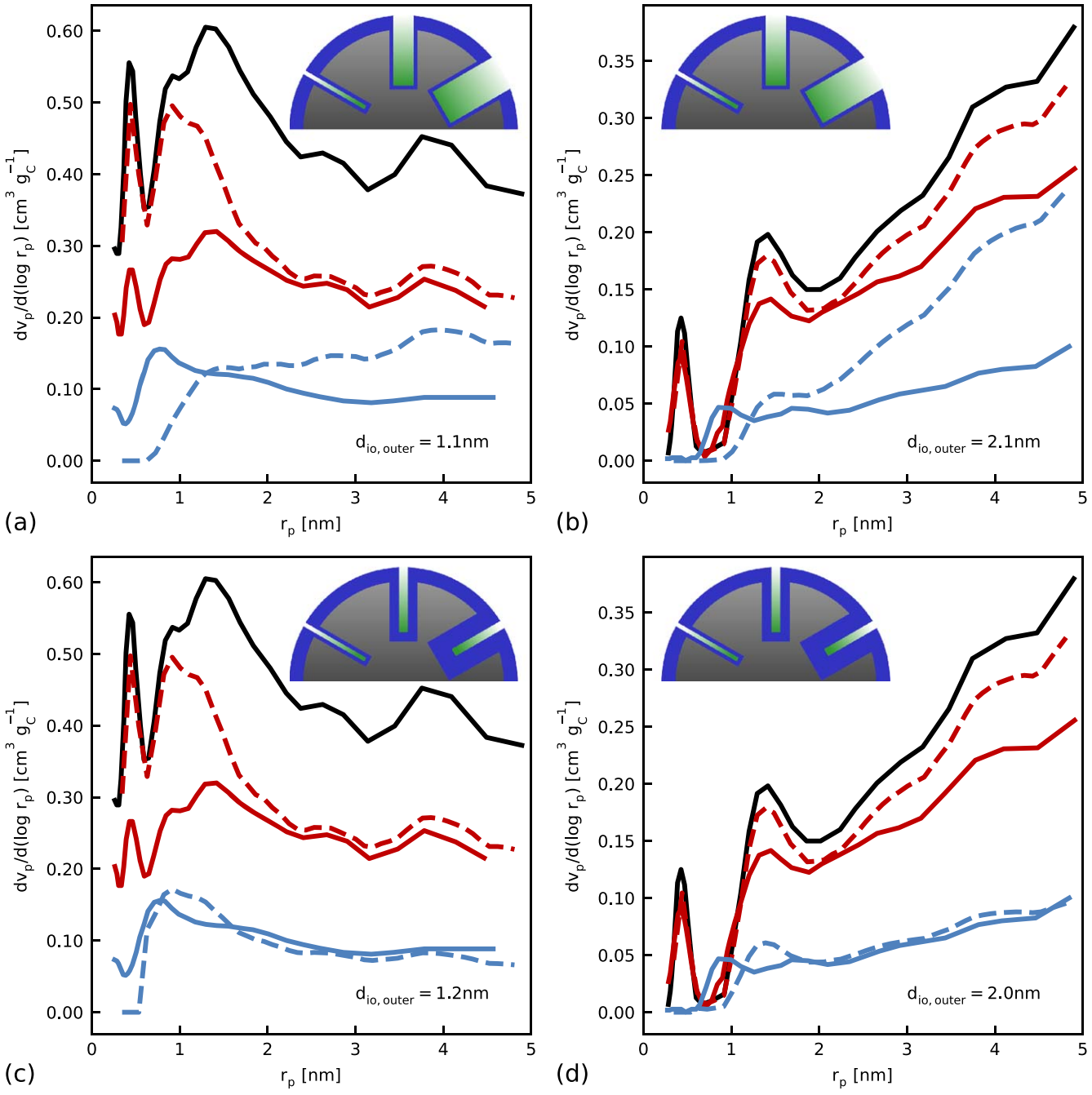

Figure 8. Measured PVDs before loading (solid black), after Pt loading (solid red) and after ionomer loading (solid blue), obtained from Ref. 1. Corresponding simulations after Pt loading (dashed red) and after ionomer loading (dashed blue) for modified ionomer loading: (a) Pt/CB and (b) Pt/GCB for $d_{io,inner} = r_{p,cut} = 0.6$ nm and the remaining ionomer attributed to $d_{io,outer}$; (c) Pt/CB and (d) Pt/GCB for $d_{io,inner} = 0.4r_p$, $r_{p,cut} = 0.6$ nm and the remaining ionomer attributed to $d_{io,outer}$. Green areas in inset schematics indicate accessible pore volume after ionomer loading.

is similar in real CCLs which encourages our distribution-based modeling approach.

Adaptation of ionomer loading in the model.—This last Section is intended to exemplify how the presented model framework can be refined to obtain good quantitative correspondence to a given support when suitable experimental information is available. For Pt/CB and Pt/GCB, the work of Park et al.[1] provides reference PVDs after ionomer loading. In Fig. 4a and 4b, we can observe that for the used parameters, the model underestimates the remaining pore volume after ionomer addition. In the experiment, ionomer addition caused pores smaller than approximately 0.6 nm to mostly vanish from the PVD. This generally agrees with our assumption of small pores being blocked entirely by ionomer while the volume of larger pores is reduced. Consequently, we would expect the calculated cutoff radius to be around 0.6 nm instead of 1.4 nm for Pt/CB and 2.0 nm for Pt/GCB. However, with the condition that $d_{io} = r_{p,cut}$ should always be the case, these are the minimal values that can be attained, having to store all given ionomer volume in the CCL. We illustrate the effects of two qualitative modifications in the model which led to much better correspondence.

A uniform thickness $d_{io} = d_{io,inner} = d_{io,outer}$ and the condition $d_{io} = r_{p,cut}$ were so far assumed in order to limit experimentally unaccessible degrees of freedom in the model to a minimum. Nevertheless, we consider it quite plausible that the inner ionomer film should be of lesser thickness than the outer film, for instance if

the ionomer film above a pore stretches and 'drips' into a pore. First, therefore, we de-coupled the outer and inner film thickness and assumed that the cutoff radius equals the inner film thickness, setting $d_{io,inner} = r_{p,cut} = 0.6$ nm. Consequently, in order to store all available ionomer in the CCL, the outer film thickness $d_{io,outer}$ must be flexible such that all ionomer which does not clad pores with $r_p > 0.6$ nm in a film of that same thickness is accomodated. Figures 8a and 8b show the corresponding PVDs and calculated $d_{io,outer}$ after ionomer loading for Pt/CB and Pt/GCB. The simulations now capture the jump in the curves around 0.6 nm well. However, for larger pores, the remaining pore volume is now overestimated. This is due to the fact that with $d_{io,inner} = r_{p,cut}$, all pores, no matter which size, are only impregnated with a rather thin film of thickness 0.6 nm with little loss of pore volume. Hence, as a further refinement, we considered it plausible that the ionomer film thickness within a pore can actually become larger when a pore is larger. If all nanopores were entirely filled with ionomer, for instance, the inner film thickness inside a pore would be equal to the respective pore radius. We therefore assumed the inner ionomer film thickness to be dependent on pore size and amount to 40% of the pore radius. This factor was motivated from the reference work of Park et al.[1] As mentioned above, the authors reported a uniform and continous ionomer coverage with a thickness of 1–2 nm or less on Pt/CB. The coverage was found to be less uniform for less porous supports, but no further quantitative information was given. The observed primary pore size range being 0.25 to 5 nm, $d_{io,inner}$ was hence set to 40% of r_p in order to obtain film thicknesses no larger than 2 nm in agreement with the observations of Park et al. The cutoff radius remained at 0.6 nm, reflecting the fact that surface tension will likely keep ionomer from dripping into the smallest pores below this size. Again, the outer ionomer film thickness was calculated such that it accounts for all ionomer not stored in the nanopores. The resultant pore volume distributions are depicted in Figs. 8c and 8d and match the experimental data very well. For both supports, the calculated outer film thickness is also within the size range of 1–2 nm.

In summary, with these exemplary considerations, we intend to illustrate that our model description of a CCL, while designed to capture the effects of the different material combinations without necessitating hard to assess parameters like the inner ionomer film thickness, still offers to control these parameters in order to obtain solid quantitative correspondence with available experimental data.

Conclusions

We presented a morphological model of the cathode catalyst layer which is able to describe established Pt/C systems and their interaction with the ionomer phase. Individual catalyst supports of varying porosity are represented by pore volume distributions. Different Pt deposition methods are accounted for by particle size distributions of Pt within primary pores and on the support surface, respectively. The distribution-based approach allows for modeled processes such as pore blockage due to Pt or ionomer impregnation of pores to be dependent on the observed particle and pore size, resulting in a pore-scale morphology which is unique to each material combination. A central assumption concerning ionomer addition is that both nanopore impregnation and blockage of the pore entrances can occur within the same CCL, the interplay of these processes having a pronounced effect on the characteristic properties of the CCL. The model provides experimentally hard to access parameters such as the ionomer film thickness, state of pore impregnation and the ionomer coverage on Pt depending on the I/C ratio, particle size and position. Further, the impact of Pt and ionomer loading on the pore volume distribution as well as global properties of the CCL such as support surface area and protonically active ECSA can be predicted.

We compared our model to six catalyst/support combinations which were characterized extensively in two recent publications[1,2] and obtained very good agreement, both qualitatively and quantitatively. In particular, the model was able to explain why the ECSA has been reported to follow a non-monotonic trend with respect to I/C on highly porous supports whereas this is not the case in less porous supports.[2] A general advantage of the model setup is that all parameters have a physical counterpart which allows to calculate a variety of relations that can be compared to measurements. Access to these parameters also allows for customizing the model such that it can describe a given CCL more accurately as was demonstrated by using an ionomer film thickness distribution within the pores rather than constant film thickness throughout the CCL. Most model Eqs. can be calculated analytically, making the simulations computationally inexpensive. We therefore suggest that our model can be integrated into existing performance or degradation models as a subroutine, allowing these models access to relevant morphological properties. For instance, the available ionomer/Pt interface could be used to assess where catalyst poisoning effects occur[18,37–39] or to investigate a possibly enhanced ionomer degradation near Pt particles.[18] Information on whether pores are blocked or impregnated by ionomer could be used to deduce the accessibility of Pt within pores for water, protons and oxygen with subsequent impact on performance. The size and number distribution of Pt on the support surface and within primary pores could be used to describe potential-induced catalyst ageing of various support types.[2,40,41] In summary, with our model, we hope to contribute a reliable translation from manufacturing parameters to CCL nanomorphology which can be employed to help account for effects of porous carbon supports on fuel cell operation.

Acknowledgments

The authors thank Toyota Research Institute for financial support of this work.

ORCID

Anne-Christine Scherzer https://orcid.org/0000-0001-9995-0302
Dietmar Gerteisen https://orcid.org/0000-0002-6419-3628

References

1. Y.-C. Park, H. Tokiwa, K. Kakinuma, M. Watanabe, and M. Uchida, *J. Power Sources*, **315**, 179 (2016).
2. A. Kobayashi, T. Fujii, C. Harada, E. Yasumoto, K. Takeda, K. Kakinuma, and M. Uchida, *ACS Appl. Energ. Materials*, **4**, 2307 (2021).
3. E. Padgett et al., *J. Electrochem. Soc.*, **165**, F173 (2018).
4. K. Malek, T. Mashio, and M. Eikerling, *Electrocatalysis*, **2**, 141 (2011).
5. S. Kamarajugadda and S. Mazumder, *J. Power Sources*, **183**, 629 (2008).
6. E. Sadeghi, A. Putz, and M. Eikerling, *J. Solid State Electr*, **18**, 1271 (2014).
7. M. Uchida, Y. Fukuoka, Y. Sugawara, N. Eda, and A. Ohta, *J. Electrochem. Soc.*, **143**, 2245 (1996).
8. T. Soboleva, X. Zhao, K. Malek, Z. Xie, T. Navessin, and S. Holdcroft, *ACS Appl. Mater. Inter.*, **2**, 375 (2010).
9. V. Yarlagadda, M. K. Carpenter, T. E. Moylan, R. S. Kukreja, R. Koestner, W. Gu, L. Thompson, and A. Kongkanand, *ACS Energy Lett*, **3**, 618 (2018).
10. R. Sun, Z. Xia, X. Xu, R. Deng, S. Wang, and G. Sun, *Nano Energy*, **75**, 104919 (2020).
11. M. Lopez-Haro, L. Guétaz, T. Printemps, A. Morin, S. Escribano, P.-H. Jouneau, P. Bayle-Guillemaud, F. Chandezon, and G. Gebel, *Nat. Commun.*, **5**, 1 (2014).
12. K. Ikeda, N. Nonoyama, and Y. Ikogi, *ECS Trans.*, **33**, 1189 (2010).
13. S. M. Andersen and L. Grahl-Madsen, *Int. J. Hydrogen Energ.*, **41**, 1892 (2016).
14. F. C. Cetinbas, R. K. Ahluwalia, N. N. Kariuki, and D. J. Myers, *J. Electrochem. Soc.*, **165**, F1051 (2018).
15. L. Chen, R. Zhang, Q. Kang, and W.-Q. Tao, *Chem. Eng. J.*, **391**, 123590 (2020).
16. A. Kusoglu and A. Z. Weber, *Chem. Rev.*, **117**, 987 (2017).
17. M.-R. Lee, H.-Y. Lee, S.-D. Yim, C.-S. Kim, Y.-G. Shul, A. Kucernak, and D. Shin, *Fuel Cells*, **18**, 129 (2018).
18. I. Martens, L. G. Melo, M. M. West, D. P. Wilkinson, D. Bizzotto, and A. P. Hitchcock, *ACS Catal*, **10**, 8285 (2020).
19. R. Darling and S. Burlatsky, *J. Electrochem. Soc.*, **168**, 054512 (2021).
20. M. El Hannach, T. Soboleva, K. Malek, A. A. Franco, M. Prat, J. Pauchet, and S. Holdcroft, *J. Power Sources*, **247**, 322 (2014).
21. Y. Hou, H. Deng, F. Pan, W. Chen, Q. Du, and K. Jiao, *Appl. Energ.*, **253**, 113561 (2019).
22. G. Inoue, T. Ohnishi, M. So, K. Park, M. Ono, and Y. Tsuge, *J. Power Sources*, **439**, 227060 (2019).
23. M. So, K. Park, Y. Tsuge, and G. Inoue, *J. Electrochem. Soc.*, **167**, 013544 (2020).
24. H. Ishikawa, Y. Sugawara, G. Inoue, and M. Kawase, *J. Power Sources*, **374**, 196 (2018).

25. Y. Wang, B. Seo, B. Wang, N. Zamel, K. Jiao, and X. C. Adroher, *Energy AI*, **1**, 100014 (2020).
26. R. M. Darling, *J. Electrochem. Soc.*, **165**, F571 (2018).
27. T. Jahnke, G. A. Futter, A. Baricci, C. Rabissi, and A. Casalegno, *J. Electrochem. Soc.*, **167**, 013523 (2019).
28. S. G. Rinaldo, J. Stumper, and M. Eikerling, *J. Phys. Chem. C*, **114**, 5773 (2010).
29. L. Hao, K. Moriyama, W. Gu, and C.-Y. Wang, *J. Electrochem. Soc.*, **162**, F854 (2015).
30. K. Meyer and P. Klobes, *Fresen. J. Anal. Chem*, **363**, 174 (1999).
31. M. Thommes, K. Kaneko, A. V. Neimark, J. P. Olivier, F. Rodriguez-Reinoso, J. Rouquerol, and K. S. Sing, *Pure Appl. Chem.*, **87**, 1051 (2015).
32. R. Alink, R. Singh, P. Schneider, K. Christmann, J. Schall, R. Keding, and N. Zamel, *Molecules*, **25**, 1523 (2020).
33. G. Sasikumar, J. Ihm, and H. Ryu, *Electrochim. Acta*, **50**, 601 (2004).
34. Z. Qi and A. Kaufman, *J. Power Sources*, **113**, 37 (2003).
35. D. Song, Q. Wang, Z. Liu, T. Navessin, M. Eikerling, and S. Holdcroft, *J. Power Sources*, **126**, 104 (2004).
36. M. Lee, M. Uchida, H. Yano, D. A. Tryk, H. Uchida, and M. Watanabe, *Electrochim. Acta*, **55**, 8504 (2010).
37. K. Kodama, A. Shinohara, N. Hasegawa, K. Shinozaki, R. Jinnouchi, T. Suzuki, T. Hatanaka, and Y. Morimoto, *J. Electrochem. Soc.*, **161**, F649 (2014).
38. T. Masuda, F. Sonsudin, P. R. Singh, H. Naohara, and K. Uosaki, *J. Phys. Chem. C*, **117**, 15704 (2013).
39. K. Shinozaki, Y. Morimoto, B. S. Pivovar, and S. S. Kocha, *J. Power Sources*, **325**, 745 (2016).
40. P. Schneider, C. Sadeler, A.-C. Scherzer, N. Zamel, and D. Gerteisen, *J. Electrochem. Soc.*, **166**, F322 (2019).
41. H. A. Baroody, D. B. Stolar, and M. H. Eikerling, *Electrochim. Acta*, **283**, 1006 (2018).